

Estimation of high-resolution dust column density maps

Empirical model fits

M. Juvela and J. Montillaud

Department of Physics, PO Box 64, University of Helsinki, 00014 Helsinki, Finland
e-mail: mika.juvela@helsinki.fi

Received 13 June 2013 / Accepted 10 July 2013

ABSTRACT

Context. Sub-millimetre dust emission is an important tracer of column density N of dense interstellar clouds. One has to combine surface brightness information at different spatial resolutions, and specific methods are needed to derive N at a resolution higher than the lowest resolution of the observations. Some methods have been discussed in the literature, including a method (in the following, method B) that constructs the N estimate in stages, where the smallest spatial scales being derived only use the shortest wavelength maps.

Aims. We propose simple model fitting as a flexible way to estimate high-resolution column density maps. Our goal is to evaluate the accuracy of this procedure and to determine whether it is a viable alternative for making these maps.

Methods. The new method consists of model maps of column density (or intensity at a reference wavelength) and colour temperature. The model is fitted using Markov chain Monte Carlo methods, comparing model predictions with observations at their native resolution. We analyse simulated surface brightness maps and compare its accuracy with method B and the results that would be obtained using high-resolution observations without noise.

Results. The new method is able to produce reliable column density estimates at a resolution significantly higher than the lowest resolution of the input maps. Compared to method B, it is relatively resilient against the effects of noise. The method is computationally more demanding, but is feasible even in the analysis of large *Herschel* maps.

Conclusions. The proposed empirical modelling method E is demonstrated to be a good alternative for calculating high-resolution column density maps, even with considerable super-resolution. Both methods E and B include the potential for further improvements, e.g., in the form of better a priori constraints.

Key words. ISM: clouds – infrared: ISM – radiative transfer – submillimeter: ISM

1. Introduction

Sub-millimetre and millimetre dust emission data are one of the main tools in the study of dense interstellar clouds (Motte et al. 1998; André et al. 2000). The large surveys of *Herschel* have provided data on many nearby molecular clouds (André et al. 2010) and on the Galactic plane (Molinari et al. 2010). Dust acts as a tracer of cloud mass, but also the intrinsic dust properties are actively investigated because they are expected to reflect the general evolution of the clouds (Ossenkopf & Henning 1994; Stepnik et al. 2003; Meny et al. 2007; Compiègne et al. 2011). The variations of dust properties can also be an important source of uncertainty in the column density estimates, but this problem is beyond the scope of the present paper.

The interpretation of dust emission data is affected by problems associated with the effects of noise and temperature variations. The noise is particularly problematic for attempts to simultaneously determine both the dust temperature and the dust emissivity spectral index β (Shetty et al. 2009a; Juvela & Ysard 2012a). Therefore, most estimates of cloud masses are derived by assuming a constant value of β . The mass estimates are always affected by temperature variations, along the line-of-sight or otherwise within the instrument beam. This tends to lead to underestimation of cloud masses (Evans et al. 2001; Stamatellos & Whitworth 2003; Shetty et al. 2009b; Malinen et al. 2011; Juvela & Ysard 2012b; Ysard et al. 2012). The effect could be estimated if the temperature structure of the source is precisely

known. In practice, detailed modelling is needed but the results still remain uncertain because the real structure of the clouds and the heating by external and internal radiation sources are not accurately known (Juvela et al. 2013a).

The calculation of column densities requires knowledge of dust temperature and the intensity of dust emission. In this paper we ignore the problems of line-of-sight temperature variations and naively assume that the colour temperature estimated from the observed intensities can be used to calculate column density. This could be called an “apparent column density” to separate it from the true column density of the source. In the following, we also use the terms temperature and column density when actually referring to colour temperature and the apparent column density.

Colour temperature can be estimated only with multiwavelength observations where the shape of the observed spectrum is sensitive to temperature. This is the case, for example, for *Herschel*, which carried out photometric observations from 70 μm to 500 μm . At the shortest wavelengths, the intensity can be significantly affected by emission from transiently heated small grains (Li & Draine 2001; Compiègne et al. 2011). Therefore, it is safer to base the estimates of the temperature and column density of large grains on data between 160 μm and 500 μm . However, the spatial resolution of these observations varies from $\sim 12''$ at 160 μm to $\sim 36''$ at 500 μm . The usual procedure is to convolve surface brightness maps to the lowest common resolution, fit the spectrum in each pixel with a modified black body law, and use the fitted intensity and colour

temperature to calculate column density estimates at the same resolution. To obtain a column density map of higher spatial resolution, one could proceed by directly deconvolving some of the maps (e.g. [Orieux et al. 2012](#)). However, the procedure is sensitive to noise and to the knowledge of the beam shapes. Therefore, the best results may not be obtained by carrying out the deconvolution for each channel independently.

[Juvela et al. \(2013a\)](#) compared two methods that can be used to derive the column density estimates at a higher resolution. The goal was to use *Herschel* data at 160–500 μm to calculate column density maps at 18'' resolution. Method A combines low-resolution colour temperature estimates with the intensity information of the 250 μm observations ([Juvela et al. 2012](#)). In method B, first proposed by [Palmeirim et al. \(2013\)](#), column density map is combined from estimates calculated using different wavelength ranges, the shortest wavelengths providing the information on the highest spatial frequencies. Method B was found to be better justified and generally quite reliable, while method A performed better in cases of a low signal-to-noise ratio (S/N). The most reliable estimates (and best resilience against noise), especially in cases of simple source geometry, was obtained by carrying out radiative transfer modelling of observations. This last option, however, is also the most complex and most time-consuming alternative.

In this paper we continue this examination, examining a new method for calculating high-resolution column density maps. The basic idea is to set up a model that consists of high-resolution maps of column density or intensity at some reference wavelength, colour temperature, and potentially also the spectral index of the dust emission. The model maps are determined by an optimisation that compares the model predictions with each of the observed surface brightness maps. Each comparison is carried out using the native resolution of the observed maps. In principle, the method is capable of reaching super-resolution. For comparison with [Juvela et al. \(2013a\)](#), we set as the goal column density maps at the same 18'' resolution. We refer to the method as “empirical modelling” to recall that it does not contain a physical model of the source, but only seeks to describe the properties of the observed intensities. Therefore, it is subject to all the errors resulting from temperature variations and from dust property variations as discussed above.

The content of the paper is the following. In Sect. 2 we present the details of the proposed new method and recount the main points of method B, which is used as the reference against which the performance of the new method is compared. In Sect. 3 we described the simulated observations that are then analysed with both methods in Sect. 4. The results are discussed in Sect. 5 before the final conclusions are presented in Sect. 6.

2. Methods

In this section we describe the two methods used to derive column density maps at a higher resolution than the lowest resolution of the input surface brightness maps. We refer specifically to the wavelengths and resolutions of *Herschel*. However, both methods can be directly applied to any similar multiwavelength data.

The column density estimates are based on the assumption that observed intensities follow a modified black body law

$$I_\nu = B_\nu(T)(1 - e^{-\tau}) \approx B_\nu(T)\tau = B_\nu(T)\kappa N, \quad (1)$$

where I_ν are the observed intensities, $B_\nu(T)$ is the Planck law for temperature T , and τ is the optical depth. The shape of the

observed spectrum fixes the colour temperature, and the optical depth can be solved from the above equation. The optical depth can be trivially scaled to column density if κ , the dust emission cross section per, e.g., hydrogen atom is known. In this paper we are not interested in the value of κ ; that is to say, the tests are actually carried out using optical depth τ . One could equally assume that the exact value of κ is known.

2.1. Method B

In [Palmeirim et al. \(2013\)](#) a higher resolution column density map was obtained by combining estimates derived using different subsets of *Herschel* wavelengths 160, 250, 350, and 500 μm . One calculates column density maps $N(250)$, $N(350)$, and $N(500)$ that are based on surface brightness maps up to the quoted wavelength, all convolved to the resolution of the quoted wavelength. When the resulting maps are convolved to a lower resolution, one obtains estimates for the new column density features that appear between the lower and the higher resolutions. We use the notation $N(\lambda_1 \rightarrow \lambda_2)$ to denote a column density map that is derived from data at wavelengths $\lambda \leq \lambda_1$ and then convolved to the resolution of observations at wavelength λ_2 . The final column density map is obtained as a combination

$$N = N(500) + [N(350) - N(350 \rightarrow 500)] + [N(250) - N(250 \rightarrow 350)], \quad (2)$$

where $N(500)$ is the best estimate of column density at low resolution, and the other terms add information on structures that become visible at progressively higher spatial resolution. Thus, Eq. (2) in principle provides a column density map at the resolution of the 250 μm observations, $\sim 18''$.

The estimates $N(250)$, $N(350)$, and $N(500)$ will be different not only because of the different resolution but also because of the noise, and bias will be different for different wavelength ranges ([Shetty et al. 2009b,a](#); [Malinen et al. 2011](#)). The biases are related to the temperature distribution of the source, which are present in real data, although not in our simulations. In particular, without data at long wavelengths, one will be relatively insensitive to very cold dust. Of course, if the estimates were identical, one could directly use the $N(250)$ map. With Eq. (2), one can include all the data, although the correction terms $[N(350) - N(350 \rightarrow 500)]$ and $[N(250) - N(250 \rightarrow 350)]$ (i.e., estimates of small-scale structures) will be progressively more insensitive to cold emission.

2.2. Empirical modelling

The principle of the proposed “empirical modelling” method (in the following, method E) is simple. One constructs a model where the free parameters correspond to maps of optical depth (or directly column density), temperature, and spectral index. In our implementation the actual parameters are the 250 μm intensity, temperature, and the spectral index. The 250 μm optical depth and the column density are obtained from Eq. (1). In this paper, we assume a constant value for the spectral index. The pixel size of these maps is selected to be smaller than the target resolution, i.e., the resolution of the estimated column density maps. The model provides high-resolution predictions of the surface brightness in all observed bands. The model (consisting of the pixel values in maps of 250 μm intensity, temperature, and possibly spectral index) is optimised by comparing observations with model predictions that are convolved down to the resolution of the observations. If some input data had much higher

resolution, they could be compared at some lower resolution that is still well sampled by the pixel size of the model maps (and is preferably better than the target resolution). Assuming that the observational errors follow normal distribution, we minimise the χ^2 value

$$\chi^2 = \sum_i^{N_\nu} \sum_j^{N_{\text{pix}}} (I_{i,j} - (M_i * B_i)_j)^2, \quad (3)$$

where $I_{i,j}$ is the observed intensity for frequency i and pixel j , M_i is the model prediction at frequency i , B_i represents the telescope beam, and the asterisk denotes the convolution operation. We use the method to analyse simulated *Herschel* observations between $160\ \mu\text{m}$ and $500\ \mu\text{m}$, and thus the number of observed frequencies is $N_\nu = 4$. The number of pixels in our model maps is $N_{\text{pix}} = 128 \times 128$ (see Sect. 3).

The resolution of the $160\ \mu\text{m}$ map is taken to be $12.0''$, and the pixel size of the model maps is set to $4.0''$. The pixel size of the model maps is independent of the pixel size of the observed maps. The only constraint is that the pixelisation should be fine enough to sample the column density at the target resolution. If the pixels are very small, the values of individual model pixels are no longer well constrained by the data, and although the model predictions match the observations at low resolution, there could be large oscillations on smaller scales. The oscillations should be suppressed with some additional regularisation, especially if the goal is to reach super-resolution. We include weak regularisation by adding a penalty to the difference between the model prediction in a single pixel compared to the convolved prediction at the observed resolution, $\Delta \ln p = -[(S_i - \langle S \rangle) / \delta S]^2$. The penalty is applied to two bands, $160\ \mu\text{m}$ and $250\ \mu\text{m}$, to constrain both temperature and column density variations. The penalty is calculated with $\delta S = 1.0$ (in the units of the simulated surface brightness, e.g. Fig. 1) and, combined with the small pixel size, turns out to have little effect on the solution.

We solve the model parameters with Markov chain Monte Carlo (MCMC) calculations that also provide full posterior probability distributions for the solved $250\ \mu\text{m}$ intensity I_{250} , temperature, and for spectral index if that were included as a free parameter. The probability distribution of $\tau(250\ \mu\text{m})$ can be computed by registering the values of the ratio $I_{250}/B_{250}(T)$. We use flat priors that restrict the temperature values to the range of 6–30 K and force the solution to have non-negative column density. The calculations are quite time-consuming because, on each step of the MCMC chain, several maps of model-predicted surface brightness need to be convolved to the observed resolutions. In the case of the simulations, we can check convergence (proper burn-in) using not only the changes of the χ^2 values but also the absolute values. The reduced χ^2 values were below 2.0 before the final runs where the model estimates were obtained as averages over 50 000 MCMC steps.

3. Simulated observations

Our goal is to estimate, based on given observed intensities, how good the methods presented in Sect. 2 are in recovering high-resolution estimates of the apparent column density. We are interested in the relative performance at different noise levels, but differences between the apparent and the real column density are beyond the scope of this study (see Sect. 1). Therefore, we can use simple simulations, and the methods can be evaluated entirely based on their ability to reproduce the results that would be obtained with noiseless observations at a given resolution.

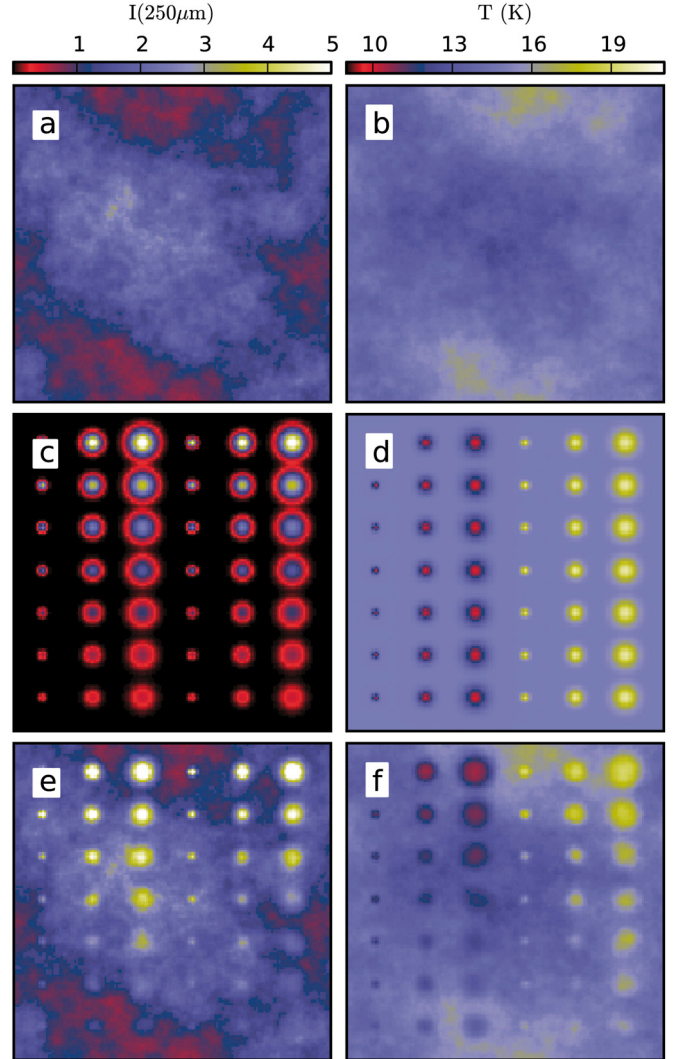


Fig. 1. Simulated data used in the tests. The $250\ \mu\text{m}$ surface brightness (left frames, arbitrary units) and the temperature (right frames) are shown for the three basic test cases. Shown are the maps for test cases with diffuse field (frames a), b), compact sources with radial temperature variations (frames c), d), and isothermal compact sources on diffuse background (frames e), f).

We simulated three sets of surface brightness maps, each with different amounts of noise. The spectral index is fixed to a constant value of 1.8. The first set of maps represents a general fluctuating intensity field. Data are generated by scaling the amplitudes of the Fourier elements of $250\ \mu\text{m}$ surface brightness and dust temperature as $\sim k^{-1.5}$ where k is the spatial frequency. After randomising the phases and transforming the data back to real space, suitable scaling results in the I_{250} maps shown in the uppermost frames of Fig. 1.

The second set of maps represents a series of compact isothermal sources with different sizes and intensities. The radial column density profile of each source is Gaussian. The temperatures are fixed to 10 K for one half of the sources and to 20 K for the second half. For each temperature, there are three columns of sources with full width at half maximum (FWHM) sizes 10.0, 20.0, and 30.0 arcsec (see Fig. 1). The rows of sources correspond to changes in the $250\ \mu\text{m}$ peak intensity by a factor of 1.5. We examine similar sources separately with radial temperature variations. The temperatures follow similar Gaussian profiles to the column density. Instead of being constant 10 K or 20 K, the

temperature changes from 15 K in the outside to 10 K or 20 K at the centre (Figs. 1 c–d).

The final set of test maps is the combination of the isothermal sources and a diffuse background with variations in both intensity and temperature (Figs. 1 e–f). The intensity maps are obtained by adding together the intensities of the previous diffuse background maps and isothermal sources. Figure 1 shows the colour temperature estimated from those intensities. However, because of the addition of modified black body spectra at two different temperatures, the resulting spectra are in fact no longer pure modified black bodies.

We add Gaussian noise to each of the simulated surface brightness maps. The default noise values are 0.15, 0.05, 0.022, and 0.02 units at $160\mu\text{m}$, $250\mu\text{m}$, $350\mu\text{m}$, and $500\mu\text{m}$. These are the noise values at the resolution of the simulated observations, 12.0, 18.3, 24.9, and 36.3 arcsec, respectively. The units are arbitrary but correspond to the surface brightness units in our simulations (e.g., in Fig. 1). In real *Herschel* observations, a cold high column density cloud can produce a surface brightness of $I(250\mu\text{m}) \sim 100 \text{ MJy sr}^{-1}$, while the typical noise value is $\sim 2 \text{ MJy sr}^{-1}$, giving a S/N of ~ 50 (see e.g. Juvela et al. 2012; Kirk et al. 2013). In our simulations a typical S/N with the default noise values is similarly $\sim 2.5:0.05 = 50$ (in model B the signal goes to zero outside the sources). In the following section, we examine cases where the noise is scaled with a factor $k_n = 0.1\text{--}3.0$ relative to the default values given above.

4. Results

4.1. Diffuse field

The first tests were done with a diffuse field that has a complex structure in both intensity and temperature and, consequently, in column density (see Fig. 1 a–b). Figure 2 compares the column density estimates that are derived with methods B and E. As in all the following tests, the observations consist of data at $160\text{--}500\mu\text{m}$.

At the noise level $k_n = 0.3$, method B gives slightly lower scatter than method E (0.007 vs. 0.009 units). Method E values are to some extent affected by Monte Carlo noise because the presented values are averaged over only 50 000 MCMC steps. Both methods recover the true column density without noticeable bias. For the higher noise case, $k_n = 3.0$, the situation is reversed and the results of method E have an rms error of 0.073 units compared to 0.083 units for method B. This is to be expected because, by also using column density estimates calculated from fewer frequency bands, method B should be more sensitive to noise. Even with $k_n = 3.0$, the $250\mu\text{m}$ S/N is still above 13 everywhere in the maps.

4.2. Compact sources

We examine isothermal compact sources with zero background next. Figure 3 shows the overall correlations between the true column density and the estimates derived with methods B and E. Unlike the previous case, the signal goes to zero outside the compact sources; i.e., a large fraction of the maps has S/N below one. In Fig. 3 we also indicate the pixels in the $T = 10 \text{ K}$ sources and in the $T = 20 \text{ K}$ sources with different colours. These differ especially regarding the $160\mu\text{m}$ data where the colder temperature leads to significantly lower signal. For $k_n = 0.3$, the two methods give comparable results for the warm sources, while for the colder sources method B results in a much larger scatter. The MCMC calculations were started with the observed $250\mu\text{m}$

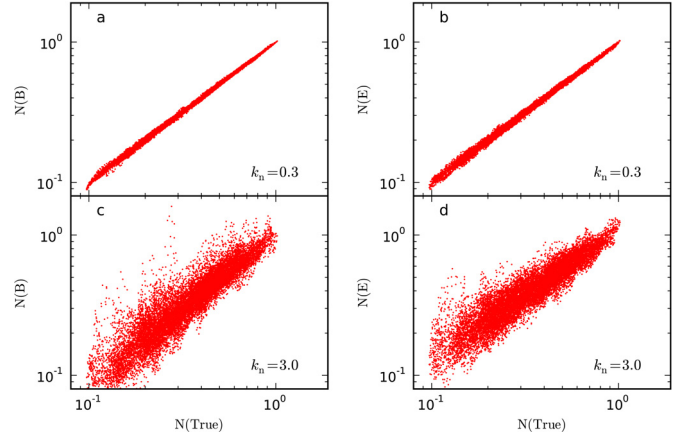


Fig. 2. Correlations between the column densities estimated with methods B and E and the column densities derived from noiseless data with a uniform resolution of $18.3''$ at all wavelengths $160\text{--}500\mu\text{m}$. The data correspond to a diffuse field with column density and temperature fluctuations.

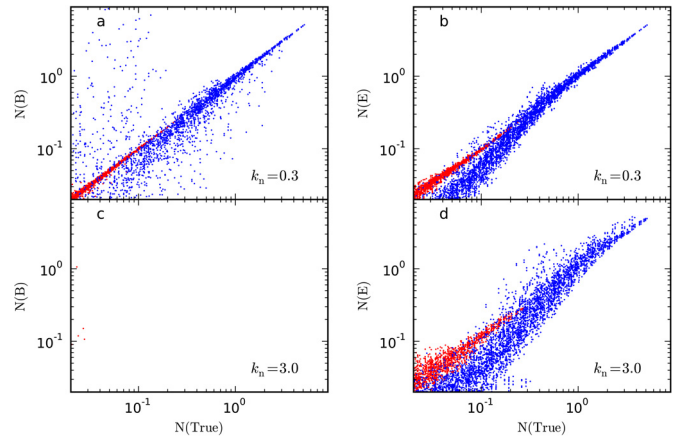


Fig. 3. Pixel-by-pixel correlations between the column density estimates of methods B and E and the column densities derived from noiseless data with a uniform resolution of $18.3''$. The observations correspond to isothermal sources at 10 K (blue points) and 20 K (red points).

surface brightness and a constant temperature of 15 K. For the 20 K sources the calculations have converged to a good solution. However, for the 10 K sources, because of the lower S/N, the values are affected by the temperature priors. The temperature prior forces temperatures in the range between 6 K and 30 K. The 6 K limit and the large temperature uncertainties bias the MCMC estimates so that the mean values from the MCMC calculation are mainly above the correct value of 10 K. Consequently, the recovered column density values are systematically too low, and this produces the bias seen in Fig. 3. It is for the same pixels that method B exhibits a very large scatter. The same trend extends to the case with $k_n = 3.0$. However, method B is no longer able to produce reasonable estimates even for the 20 K sources.

Figure 4 shows the situation in map form for the $k_n = 0.3$ case. In this figure, we have masked in the result maps all regions where the $250\mu\text{m}$ surface brightness drops below the $1\text{-}\sigma$ noise value. Within the unmasked area, the rms error of method B column density estimates is 0.15, compared to 0.06 for method E. As the value of k_n is increased, the difference between the methods increases rapidly. As mentioned above, part of this may be attributed to the fact that, even in the absence of observations

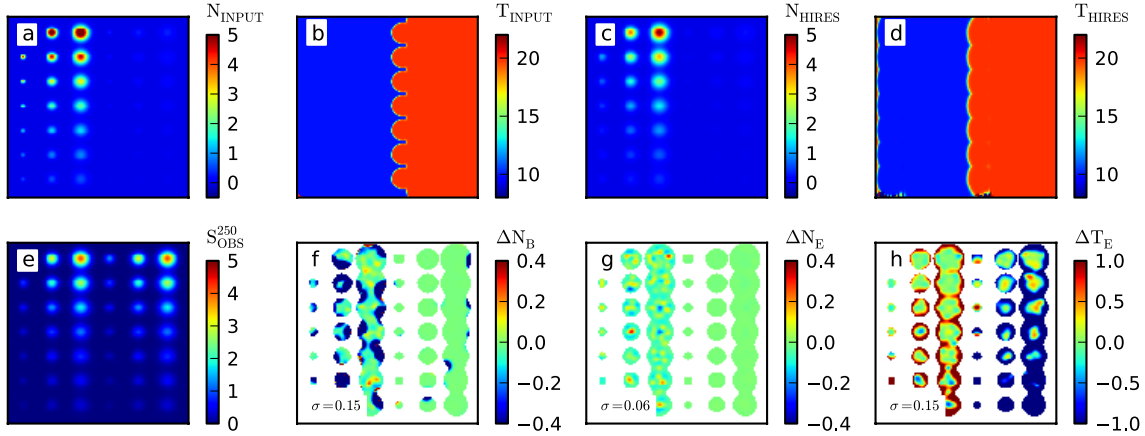


Fig. 4. Results for the test with isothermal compact sources with noise $k_n = 0.3$. Shown are the input model of column density (frame **a**) and temperature (frame **b**), the corresponding parameters extracted from noiseless data at $18.3''$ resolution (frames **c**, **d**), the observed $250 \mu\text{m}$ surface brightness (frame **e**), the absolute errors of the column density estimates of method B (frame **f**), and the absolute errors of the column density and temperature determined with method E (frames **g** and **h**). In the last three frames, the rms error of the corresponding parameter is given in the figure.

of significant S/N, the temperature of method E remains constrained by the priors.

We separately tested the accuracy with which the parameters of the radial column density profiles of the sources were recovered. Based on the known locations of the Gaussian sources, we fitted the column density estimates with two-dimensional Gaussian surfaces. The values were compared not to the input values of the simulations but to the values that would be recovered in the absence of observational noise, using $18.3''$ resolution data at all four frequencies. Each fit was carried out with data up to a distance equal to FWHM from the source centre.

The injected sources have FWHM values of 10.0, 20.0, and 30.0 arcsec. Because of the convolution with the $18.3''$ beam, the extracted FWHM values should be equal to $20.9''$, $27.1''$, and $35.1''$, respectively. The peak values are similarly lower than in the injected Gaussians but are compared directly with the results from idealised observations at the $18.3''$ resolution.

Figure 5 illustrates the accuracy of the recovered peak column density and FWHM values relative to these reference values. The noise corresponds to the low noise level of $k_n = 0.1$ where approximately correct values are still recovered for most of the sources. The accuracy is again better for method E, and this is particularly noticeable for the estimated FWHM values.

When the noise level is raised to $k_n = 0.3$ (Fig. 5, lower frames), some of the lower intensity sources are lost and many of the FWHM estimates of method B are already off by more than 60%. Based on Fig. 3, this already was to be expected. The difference is partly because method E simultaneously uses all wavelengths to constrain the solution. However, equally important is the technical detail that method E calculations include priors that prevent the column density estimates from exploding in the noise-dominated outer regions of the sources.

When the isothermal sources are seen against a fluctuating diffuse background, we attempt to recover the source parameters by fitting a two-dimensional Gaussian surface plus a constant background. For low values of k_n , the observations of the sources are no longer noise-limited, and all sources cannot be detected even in the noiseless maps. Therefore, in Fig. 6, we only compare the predictions of methods B and E when the noiseless $18.3''$ resolution observations recover both the peak column density and the FWHM extent of a source to a relative accuracy better than 50%. This removes most sources with the lowest peak

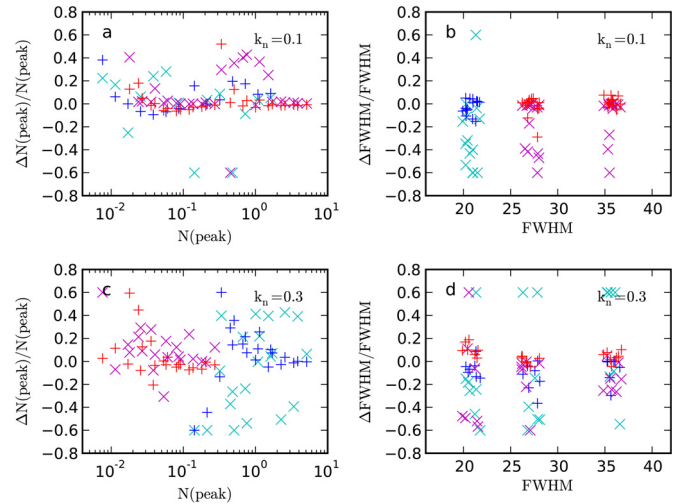


Fig. 5. Accuracy of the recovered peak column density (*left frames*) and FWHM (*right frames*) values of the compact isothermal sources. The plots show the relative errors for method B (crosses) and method E (plus signs) relative to idealised observations at $18.3''$ resolution. The colours are used to separate 10 K and 20 K sources, blue and red for method E and cyan and magenta for method B, respectively. The *upper frames* correspond to a noise level of $k_n = 0.1$, the *lower frames* to $k_n = 0.3$. Values outside the range of $[-0.6, 0.6]$ are plotted at those boundaries. In the FWHM plots, to reduce the overlap of the symbols, we have added jitter in the x -axis values.

column densities but also some of the stronger sources that are seen towards a high background.

Compared to Fig. 5, the scatter in the parameters recovered by methods B and E is decreased because of this filtering of sources. Method E appears to be more accurate in extracting the values of peak column density while, unlike in Fig. 6, the difference is small on the FWHM estimates for $k_n = 0.3$. The rms errors are very similar because these values are determined mostly by the outliers (i.e. points with relative errors above ~ 0.2) that are equally frequent for both methods.

The final test involves compact sources with radial temperature profiles. The background has a constant temperature of 15 K, and the temperature either decreases to 10 K or increases to 20 K at the centre of a source (see Fig. 1). Figures 3 and 8

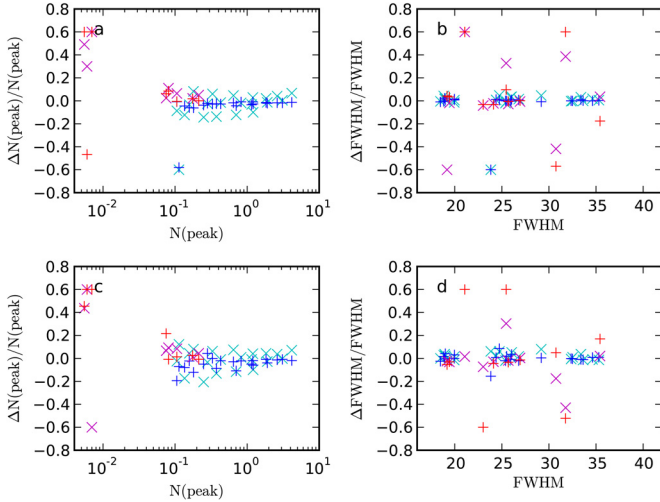


Fig. 6. Accuracy of the recovered peak column density (left frames) and FWHM (right frames) values for compact sources on fluctuating background. The plots show the relative errors for method B (crosses) and method E (plus signs) relative to idealised observations at $18.3''$ resolution. The 10 K and the 20 K sources are respectively shown as blue and red symbols for method E and as cyan and magenta symbols for method B. The upper frames correspond to a noise level of $k_n = 0.1$, the lower frames to $k_n = 0.3$. Values outside the range of $[-0.6, 0.6]$ are plotted at those boundaries.

again show the pixel-to-pixel correlations and the accuracy of the recovered Gaussian parameters in relation to idealised observations. Comparing the result to Fig. 3, the noise is actually lower, mainly because the observed temperature of the non-isothermal sources is always above 10 K. For the same reason, there is no bias in method E results where the column density of the colder sources would be systematically underestimated. In contrast, the relative error in the column density of the 10–15 K sources appears to be positive. This is not obvious for method B (possibly because of the large scatter) but is clear for method E. It could be related to the fact that, because of the higher S/N, the central part of each source has a large weight in determining the overall solution. This could be enhanced by the smoothing of the model maps but does not appear likely because of the weakness of that regularisation. In the higher S/N case, method B performs well providing actually more accurate estimates of N for the highest column density sources, again partly because of the Monte Carlo noise of method E calculations.

5. Discussion

We have compared two methods, methods B and E, that can be used to derive high-resolution column density maps from multi-frequency observations of dust emission. This study is an extension of the paper by Juvola et al. (2013a) where some methods already were discussed, including the method B. In this paper we have proposed method E, the “empirical modelling”, as a viable alternative for the task. In this method high-resolution model images of column density (or intensity at a reference wavelength) and temperature are, via convolution, matched to observations. This has the advantage that all wavelengths are used simultaneously to constrain the solution. The calculations were completed with MCMC methods, using flat priors that allowed all positive values of column density and all temperatures in the range $6 \text{ K} < T < 30 \text{ K}$.

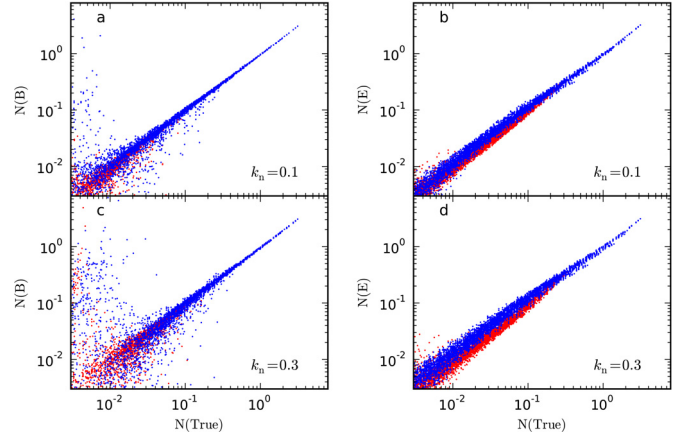


Fig. 7. Correlations between method B column density predictions (left frames) and method E column density predictions (right frames) with the values derived from noiseless data with a uniform resolution of $18.3''$. The model consists of compact sources with radially increasing or decreasing temperature. The noise levels k_n are indicated in the frames. The colours indicate the pixels in the warm sources (15–20 K, red points) and the cold sources (10–15 K, blue points).

We carried out tests with simulated observations corresponding to *Herschel* data at wavelengths between $160 \mu\text{m}$ and $500 \mu\text{m}$. The tests conducted with fields of diffuse surface brightness and with fields containing compact objects both showed that the method E provides generally more accurate results. However, the differences were mostly relatively small and became significant only when dealing with data with low S/Ns. The advantages of method E result partly from the basic nature of the method, i.e., the simultaneous fit of data at all wavelengths. In method B, the highest spatial frequencies are estimated based only on the $160 \mu\text{m}$ and $250 \mu\text{m}$ bands. This makes the method sensitive to observational noise in those channels, particularly in the case of cold dust emission for which the S/N of the $160 \mu\text{m}$ band can be low, both in our simulations and in real cold dust clouds.

The Bayesian implementation of method E is equally important. Although the priors were flat and had wide ranges of allowed values, they become important at low signal levels. This was most noticeable in tests with compact sources on zero background (e.g., Fig. 3). In the outer regions of the sources the S/N falls below one, but in method B, the column density estimates start to fluctuate strongly already well before that. In our implementation of method E, the temperature is constrained to remain above 6 K. The prior applies to all MCMC samples. For low S/Ns, the credible region of T becomes very wide. The constraint $T > 6 \text{ K}$ removes the low-temperature samples, and this can bias the Bayesian estimate, which is the average of all MCMC samples, of cold sources. The effect was seen in Fig. 3 where the column density estimates were biased downwards for most 10 K, low surface-brightness sources. However, a limit on T values is essential to avoid very low temperatures that could, in a strongly non-linear fashion, lead to very high column densities (as was the case of method B). In Fig. 3, a more liberal lower limit would reduce the bias of the temperature estimates of method E but, as shown by the corresponding results of method B, the data are clearly not enough to strongly constrain the results. This is readily seen in the MCMC error estimates of the temperature.

The radial temperature variations did not cause particular problems for either method (Figs. 7–8); i.e., the errors were not significantly larger than what would have been expected based

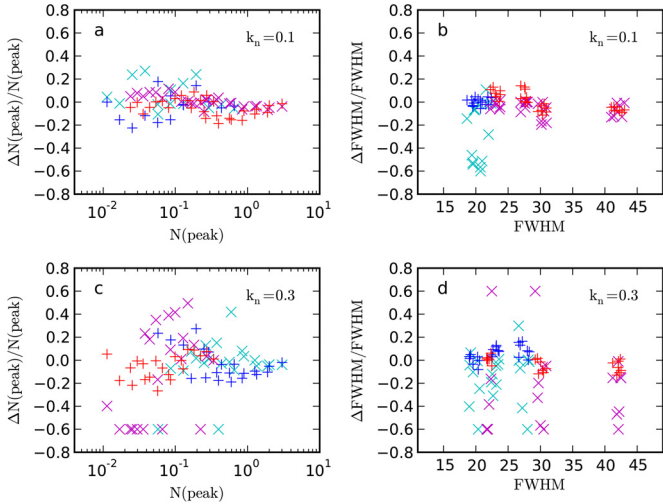


Fig. 8. Corresponding to the models in Fig. 7, the accuracy of the recovered peak column densities (*left frames*) and FWHM values (*right frames*). The relative errors of method B (cyan and magenta crosses for cold and warm sources, respectively) and method E (blue and red plus signs for cold and warm sources, respectively) are shown relative to idealised observations at $18.3''$ resolution. The noise levels k_n are indicated in the frames. Values with relative errors outside the range of $[-0.6, 0.6]$ are plotted at those boundaries. To reduce overlap between plot symbols, some jitter was added to the x -coordinate values of the FWHM plots.

on the tests with isothermal sources. There was only a weak indication of a possible bias that may affect column density estimates in the outer parts of the sources.

Method E compares a high-resolution model with observation through convolution and is thus essentially a deconvolution method. We defined the models at $4''$ pixels, and the model predictions were convolved to a $18.3''$ resolution for comparison with method B. The final resolution can be selected freely as long as it is lower than the resolution of the model itself. However, because deconvolution amplifies the noise, the solution becomes more uncertain with higher target resolution, and the solution may need additional regularisation to avoid unphysical oscillations. So far, the regularisation consisted of the priors, and a small penalty that was attached to surface brightness changes between the neighbouring pixels of the full-resolution model predictions. Because many of the observations existed at or close to the target resolution, there is still little need for regularisation as long as the S/N is high.

As a final test, we calculated model predictions at $12.0''$ resolution. Apart from the change in resolution, the test corresponds to that of Fig. 3. The results of method E were compared with parameters that would be obtained with noiseless observations where the resolution is $12.0''$ at all wavelengths. Figure 9 shows the pixel-to-pixel correlations. Compared to the lower resolution results in Fig. 3, the noise is, of course, higher because the noise per resolution unit is more than 50% higher. The errors are still small for the 20 K data and (as relative errors) for all high column density pixels. In other words, the peak column densities are recovered with good accuracy even at $12.0''$ resolution. Figure 10 directly compares the accuracy of the recovered peak column density and FWHM values that are obtained from fitting the sources with 2D Gaussian surfaces. At $k_n = 0.1$, $1-\sigma$ relative errors are 18% and 11% for column density and FWHM, respectively. These values are again raised by a small number of outliers (these, however, are clipped to the range of $\pm 60\%$ relative

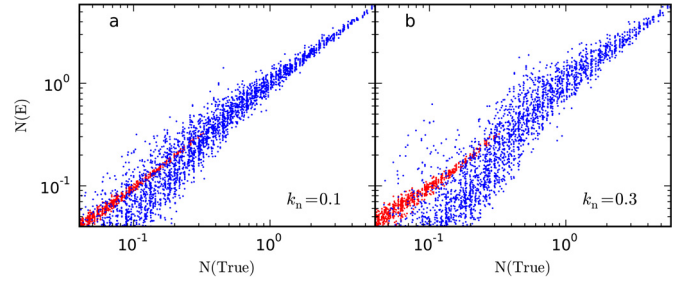


Fig. 9. Correlations between the column density estimates of method E and the corresponding values derived from noiseless data with a uniform resolution of $12.0''$. The noise levels k_n are given in the figure. The blue and the red points correspond, respectively, to pixels in 10 K and in 20 K sources.

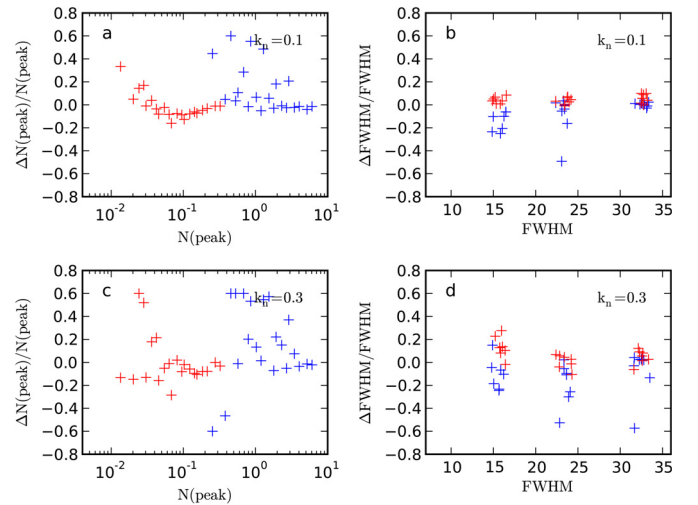


Fig. 10. Accuracy of the recovered peak column density (*left frames*) and FWHM (*right frames*) values for compact sources, estimated with method E at the resolution of $12.0''$. The *upper frames* correspond to a noise level of $k_n = 0.1$ and the lower frames to $k_n = 0.3$. The blue and the red symbols correspond, respectively, to the 10 K and 20 K sources. Values outside the range of $[-0.6, 0.6]$ are plotted at those boundaries. To reduce the overlap of plot symbols, some jitter has been added to the x -axis values of the FWHM plots.

errors, similar to Fig. 10) and most errors are below 10% (69% and 83% for column density and FWHM, respectively).

Based on the conducted tests, we can conclude that method E is a viable alternative for deriving high-resolution column density maps from observations, such as those conducted with *Herschel*. One of the main downsides of the method is its computational cost that is an issue, regardless of whether the method is implemented as an MCMC calculation (as in this paper) or as a direct optimisation problem. For accurate estimation of the uncertainties, MCMC is the better, although slower alternative. The main cost is caused by, on each iteration, the model predictions needing to be convolved to each resolution of the observations. In the tests in this paper, this meant that 128×128 pixel surface brightness maps were convolved to four different resolutions (corresponding to $160 \mu\text{m}$, $250 \mu\text{m}$, $350 \mu\text{m}$, and $500 \mu\text{m}$ measurements). The burn-in and the proper sampling of the credible region both required some tens of thousand MCMC steps. This resulted in a Monte Carlo noise that, however, was not completely negligible at small k_n (e.g., Fig. 3). The calculations can be sped-up by using GPUs for the convolutions. Nevertheless, the calculation times are several hours in

wall-clock time, depending somewhat on the selected initial conditions. We started all runs with a constant temperature of 15 K, but the burn-in phase could be shortened by using, for example, the results of method B as the starting point. With $4.0''$ pixel size, the analysed maps corresponded to an area of $\sim 8.5' \times 8.5'$. This means that the analysis of one-degree-sized maps could take several days. Although long, this can still be considered feasible. The convolution makes the problem non-local; i.e., model parameters depend on each other over distances defined by the largest beam of observations. However, the observations could easily be divided into patches that could be processed in parallel.

In the tests the dust emission spectral index β was assumed to be constant. It is straightforward to include variable β in the model by defining the model through maps of column density, temperature, and spectral index. Because of the natural anticorrelation of T and β in the modified black body fits, this would significantly increase the scatter in the estimated temperatures (Shetty et al. 2009a; Juvela & Ysard 2012a; Juvela et al. 2013b) and in N . Therefore, it might be necessary to constrain the solutions more strongly, e.g., by effectively determining the spectral index only at a lower resolution. However, this is not an optimal solution because the (apparent) spectral index can change even on small scales, in association with local heating sources (Malinen et al. 2012; Juvela et al. 2011). It would be better to restrict the use of strong regularisation to regions of low surface brightness. This could be implemented within the framework of hierarchical models that also would allow the inclusion of a wide range of other constraints (Kelly et al. 2012; Juvela et al. 2013b).

We carried out preliminary tests that showed that, if allowed by the S/N, method E can be used directly for super-resolution, reaching scales below those directly accessible to method B. More investigations would be needed to quantify the performance and to find out whether the results could be further improved, e.g., with more realistic priors. Further work also should be done on the method B. It may be possible to significantly reduce its sensitivity to noise simply by using constrained optimisation, e.g., by effectively adopting similar priors as were already used in method E.

6. Conclusions

We have proposed “empirical modelling” as method E, for estimating high-resolution column density maps. As such, this conceptually straightforward method can be used whenever observations of different resolutions need to be combined. In this paper, the method was applied to simulated dust emission observations that correspond to different resolution *Herschel* measurements at wavelengths between $160\mu\text{m}$ and $500\mu\text{m}$. The method was compared to another method, called here method B, which was presented by Palmeirim et al. (2013) and further discussed

in Juvela et al. (2013a). The tests lead to the following conclusions.

- For high S/N data, both methods provide reliable column density estimates at the $\sim 18''$ resolution of $250\mu\text{m}$ data.
- Method B is more sensitive to noise. This also complicates the analysis of compact objects because of the strong column density fluctuations towards the outer parts of the sources.
- Method E is more time-consuming but gives consistently more reliable estimates. The use of GPU computing makes the method feasible for analysing large maps.
- Radial temperature variations has no significant effect on the accuracy of the column density estimates of either method.
- With data of sufficient S/N, method E can be used directly for even higher resolution estimates. This was demonstrated by estimating column densities at $12''$ resolution.
- Further improvements should be possible in both methods. For method E, the super-resolution estimates may be improved with better regularisation. For method B, constrained optimisation can mitigate the problems encountered at low S/N levels.

Acknowledgements. The authors acknowledge the support of the Academy of Finland grant No. 250741.

References

- André, P., Ward-Thompson, D., & Barsony, M. 2000, *Protostars and Planets IV*, 59
- André, P., Men'shchikov, A., Bontemps, S., et al. 2010, *A&A*, 518, L102
- Compiègne, M., Verstraete, L., Jones, A., et al. 2011, *A&A*, 525, A103
- Evans, II, N. J., Rawlings, J. M. C., Shirley, Y. L., & Mundy, L. G. 2001, *ApJ*, 557, 193
- Juvela, M., & Ysard, N. 2012a, *A&A*, 541, A33
- Juvela, M., & Ysard, N. 2012b, *A&A*, 539, A71
- Juvela, M., Ristorcelli, I., Pelkonen, V.-M., et al. 2011, *A&A*, 527, A111
- Juvela, M., Ristorcelli, I., Pagani, L., et al. 2012, *A&A*, 541, A12
- Juvela, M., Malinen, J., & Lunttila, T. 2013a, *A&A*, 553, A113
- Juvela, M., Montillaud, J., Ysard, N., & Lunttila, T. 2013b, 556, A63
- Kelly, B. C., Shetty, R., Stutz, A. M., et al. 2012, *ApJ*, 752, 55
- Kirk, J. M., Ward-Thompson, D., Palmeirim, P., et al. 2013, *MNRAS*, 432, 1424
- Li, A., & Draine, B. T. 2001, *ApJ*, 554, 778
- Malinen, J., Juvela, M., Collins, D. C., Lunttila, T., & Padoan, P. 2011, *A&A*, 530, A101
- Malinen, J., Juvela, M., Rawlings, M. G., et al. 2012, *A&A*, 544, A50
- Meny, C., Gromov, V., Boudet, N., et al. 2007, *A&A*, 468, 171
- Molinari, S., Swinyard, B., Bally, J., et al. 2010, *A&A*, 518, L100
- Motte, F., André, P., & Neri, R. 1998, *A&A*, 336, 150
- Orieux, F., Giovannelli, J.-F., Rodet, T., et al. 2012, *A&A*, 539, A38
- Ossenkopf, V., & Henning, T. 1994, *A&A*, 291, 943
- Palmeirim, P., André, P., Kirk, J., et al. 2013, *A&A*, 550, A38
- Shetty, R., Kauffmann, J., Schnee, S., & Goodman, A. A. 2009a, *ApJ*, 696, 676
- Shetty, R., Kauffmann, J., Schnee, S., Goodman, A. A., & Ercolano, B. 2009b, *ApJ*, 696, 2234
- Stamatellos, D., & Whitworth, A. P. 2003, *A&A*, 407, 941
- Stepnik, B., Abergel, A., Bernard, J., et al. 2003, *A&A*, 398, 551
- Ysard, N., Juvela, M., Demyk, K., et al. 2012, *A&A*, 542, A21